Assessment of the Energy Consumption and Drivability Performance of an IPMSM-Driven Electric Vehicle Using Different Buried Magnet Arrangements

energies

MDPI

Article

Assessment of the Energy Consumption and Drivability Performance of an IPMSM-Driven Electric Vehicle Using Different Buried Magnet Arrangements

Pedram Asef [1,*], Ramon Bargallo [2], Andrew Lapthorn [3], Davide Tavernini [4], Lingyun Shao [4] and Aldo Sorniotti [4]

1 Department of Engineering and Technology, University of Hertfordshire, Hatfield AL10 9AB, UK
2 Department of Electrical Engineering, Polytechnic University of Catalonia, 08019 Barcelona, Spain; ramon.bargallo@upc.edu
3 Department of Electrical and Computer Engineering, University of Canterbury, Christchurch CT1 1QU, New Zealand; andrew.lapthorn@canterbury.ac.nz
4 Department of Mechanical Engineering Sciences, University of Surrey, Guildford GU2 7XH, UK; d.tavernini@surrey.ac.uk (D.T.); l.shao@surrey.ac.uk (L.S.); a.sorniotti@surrey.ac.uk (A.S.)
* Correspondence: p.asef@herts.ac.uk

Abstract: This study investigates the influence of the buried magnet arrangement on the efficiency and drivability performance provided by an on-board interior permanent magnet synchronous machine for a four-wheel-drive electric car with two single-speed on-board powertrains. The relevant motor characteristics, including flux-linkage, inductance, electromagnetic torque, iron loss, total loss, and efficiency, are analyzed for a set of six permanent magnet configurations suitable for the specific machine, which is controlled through maximum-torque-per-ampere and maximum-torque-per-voltage strategies. Moreover, the impact of each magnet arrangement is analyzed in connection with the energy consumption along four driving cycles, as well as the longitudinal acceleration and gradeability performance of the considered vehicle. The simulation results identify the most promising rotor solutions, and show that: (i) the appropriate selection of the rotor configuration is especially important for the driving cycles with substantial high-speed sections; (ii) the magnet arrangement has a major impact on the maximum motor torque below the base speed, and thus on the longitudinal acceleration and gradeability performance; and (iii) the configurations that excel in energy efficiency are among the worst in terms of drivability, and vice versa, i.e., at the vehicle level, the rotor arrangement selection is a trade-off between energy efficiency and longitudinal vehicle dynamics.

Keywords: AC machines; electromagnetic analysis; electric vehicles; energy consumption; longitudinal acceleration; finite element analysis; permanent magnet machines

Citation: Asef, P.; Bargallo, R.; Lapthorn, A.; Tavernini, D.; Shao, L.; Sorniotti, A. Assessment of the Energy Consumption and Drivability Performance of an IPMSM-Driven Electric Vehicle Using Different Buried Magnet Arrangements. *Energies* **2021**, *14*, 1418. https://doi.org/10.3390/en14051418

Received: 6 February 2021
Accepted: 28 February 2021
Published: 4 March 2021

1. Introduction

In recent years, interior permanent magnet synchronous machines (IPMSM) have been widely used for electric vehicle (EV) powertrains [1,2], due to their superior electromagnetic performance, e.g., in terms of high airgap-flux and power densities, low rotor losses, and high efficiency for a wide speed range. Because of the variety of operating conditions of electric powertrains, the electromagnetic maps of the motors are essential tools for designing and evaluating the drives, and have been widely used in the literature [3–5].

In IPMSMs, the rotor is the most complex part, because of the permanent magnet (PM) arrangement and its effect on the overall electromagnetic performance. The buried design of the magnets prevents their separation from the rotor, despite the significant centrifugal force at high speed, and produces a hybrid torque, combination of magnet and reluctance contributions, which results in high efficiency [6]. Many complex magnet arrangements have been proposed for achieving specific characteristics [7–9].

References [7–13] discuss the performance improvement of IPMSMs, associated with various magnet arrangements and shaping techniques. For example, in [10], Kim et al. investigate the demagnetization performance of permanent magnets within three kinds of rotor types for IPMSMs, as well as the resulting motor performance in terms of rated torque, output current, and efficiency. In [11], Cirani et al. consider a novel rotor design for IPMSMs. The advantage of their solution is a major reduction in magnetic flux leakage in the rotor iron bridges, which represents the main limitation of this machine topology. Kano [12] studies a novel flux barrier design for torque ripple reduction in saliency-based sensorless drive concentrated-winding IPMSMs. Zhu et al. [13] adopt magnet shaping techniques to improve the torque capability in brushless AC (alternating current) machines, by optimizing the third order harmonic in an arrangement with inverse cosine shape airgap and sinusoidal shape magnet, which results in 11% average torque increase.

The literature extensively analyzes the influence of the electric motor topology on the resulting efficiency maps [14]. Several methodologies have been proposed for generating efficiency maps, with the purpose of predicting the system performance through vehicle simulations, and select the drive/s accordingly [3,4,14]. For example, in [15], the motor efficiency map is generated from a time-domain two-dimensional (2-D) finite element analysis (FEA) model in ANSYS Maxwell, which calculates the d- and q-axis currents, and is coupled with a multi-objective optimization. During high-speed EV operation, IPMSMs are typically subject to flux weakening; in this condition, the motor iron loss, more precisely the eddy-current loss, tends to significantly increase, thus reducing efficiency. In [16], Mohammadi and Lowther consider the 2010 Toyota Prius IPMSM and a PM-assisted synchronous reluctance machine, and use nonlinear motor control formulations, i.e., maximum-torque-per-ampere (MTPA), flux weakening, and maximum-torque-per-voltage (MTPV), in the computation of the efficiency maps, while accounting for both saturation and cross-coupling effects. MTPA and MTPV algorithms [17–24] are widely used to enhance the efficiency and control performance of IPMSMs, below and above the base speed, respectively. These strategies can be implemented through offline-generated maps, reducing the online computational burden but increasing the memory requirements, or through online optimization. The conventional optimality criteria for MTPA and MTPV do not consider magnetic core saturation, and therefore result in deviations from the optimal trajectory, especially at higher load currents. Recent research [25] proposes mathematical formulations to account for magnetic core saturation in the MTPA and MTPV criteria, and obtains the corresponding optimal solutions.

Although the available literature discusses various PM arrangements for EV traction motors [14], to the best of the authors' knowledge there is a lack of comprehensive comparisons of the resulting motor efficiency characteristics, and evaluations of the implications at the EV level, e.g., in terms of energy consumption during driving cycles and drivability performance. For a case study IPMSM for a four-wheel-drive EV with two single-speed on-board powertrains, this research targets the identified gap with the following main novel contributions:

- Simulation analysis, mapping, and comparison of the electromagnetic characteristics of the IPMSM with six of the most common buried magnet arrangements, for the same target magnet volume, demagnetization rating, rotor yoke volume per magnet volume, and stator configuration;
- Comparison of the resulting EV energy consumption along a comprehensive set of driving cycles, as well as drivability performance, and identification of the most suitable rotor configurations.

The remainder of the manuscript is organized as follows: Section 2 presents the considered IPMSM rotor topologies and their parametric design process; Section 3 describes the adopted analytical models; Section 4 compares the motor maps; Section 5 analyzes the EV energy efficiency and drivability performance, and is followed by the conclusions.

2. Considered Rotor Configurations

The simulated three-phase IPMSM with inner rotor topology has 48 slots and 8 poles, with a total mass of 10.5 kg. Each phase has 110 conductors, with a net fill factor equal to 0.51. The magnet and core materials are NdFeB and M330-35A, respectively. Figure 1 presents the three-phase winding distribution of the stator, and the slot-related parameters (given in Figure 1b), while Table 1 reports the geometric stator specifications, which are the same for all considered arrangements. Figure 1c shows the rotor parameters. The rotor arrangements depend on the PM layouts, which affect the electromagnetic behavior of the machines. For a fair comparison, the total PM volume, V_m, of the considered configurations is identical, and set to 24 cm^3. All magnets are radially magnetized.

Figure 2 illustrates the considered PM arrangements, commonly investigated by researchers, e.g., see [10,11,13,26–41], in a cross-sectional view: (i) a rectangular magnet with a rectangular and open window (referred to as R-ROW in the remainder) [10,26,27], see Figure 2a; (ii) an arrangement similar to the previous one, but with a semicircular open window (R-SOW) [11], see Figure 2b; (iii) a rectangular magnet with an isosceles-trapezoid-shaped open window (R-IOW) [28–33], see Figure 2c; (iv) two separate rectangular magnets, divided by a central leg, with a semicircular open window (RCL-SOW), similarly to [35–37], see Figure 2d. The material used in the central leg is the same as for the rotor yoke; (v) a rectangular magnet with a central leg, and an isosceles-trapezoid-shaped open window (RCL-IOW) [34,38,40], see Figure 2e; and (vi) an irregular hexagonal magnet (known as bread loaf), with no open window (H-NOW) [13], see Figure 2f.

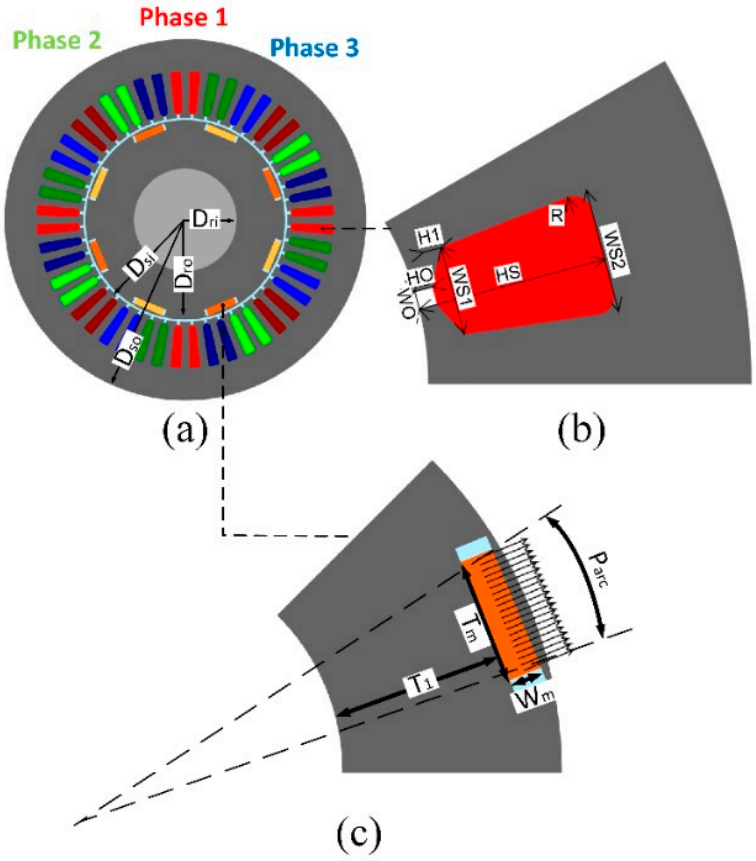

Figure 1. (**a**) Three-phase winding distribution in the stator core, (**b**) slot dimensions, and (**c**) rotor parameters.

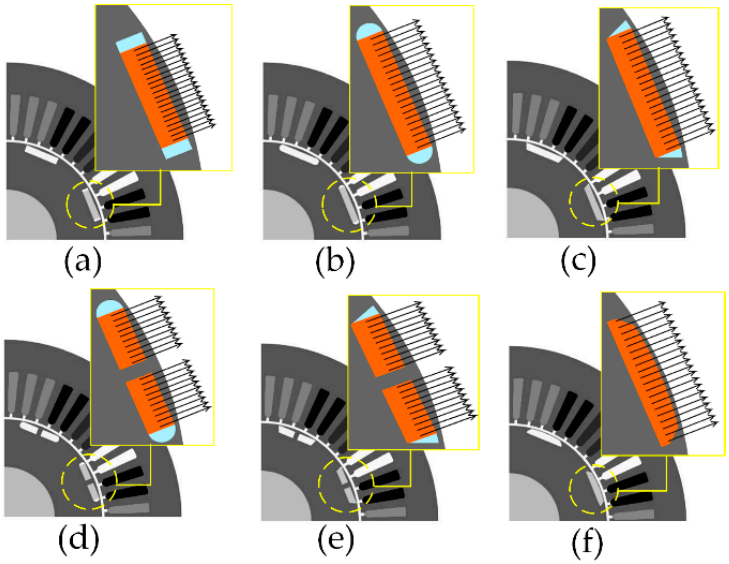

Figure 2. Qualitative layout of the considered rotor magnet arrangements: (**a**) R-ROW, (**b**) R-SOW, (**c**) R-IOW, (**d**) RCL-SOW, (**e**) RCL-IOW, and (**f**) H-NOW. Each subplot represents two of the eight poles of the rotor.

The first three magnet arrangements, i.e., R-ROW, R-SOW, and R-IOW, use different shapes of the open windows to reduce the leakage flux at both ends of the magnet. The second and third arrangements are more practical than the first one from the viewpoint of the manufacturing process to fix the magnets. The central legs in RCL-SOW and RCL-IOW improve the ratio of reluctance torque to magnet torque and saliency, in addition to reducing the cogging torque. Although they increase the leakage flux, the higher *d*-axis inductance can improve the flux weakening capability. The last magnet arrangement, H-NOW, is designed to exploit the harmonic components of the magnetomotive force and permeance.

Table 1. Main stator parameters.

Parameter	Description	Unit	Value
D_{si}	Inner stator diameter	mm	178
D_{so}	Outer stator diameter	mm	318
H_s	Slot height	mm	41
H_o	Height of the slot opening	mm	4.0
H_1	Intermediary height of the slot width	mm	2.2
L	Axial length	mm	84
L_g	Airgap length	mm	0.8
N_s	Number of slots	-	48
R	Fillet radius	mm	1.3
V	Undercut angle of stator tooth tip	deg	41
W_{s1}	Bottom slot width	mm	6.3
W_{s2}	Top slot width	mm	8.8
W_{T1}	Tooth width, upper part of slot	mm	6.2
W_{T2}	Tooth width, bottom part of slot	mm	6.2
W_o	Width of slot opening	mm	1.3

Figure 3 presents the effect of the main geometric magnet parameters, i.e., magnet width and pole arc. The sensitivity analysis, using the design of experiment/regression (DOE/R) method [42], shows that the increase in the pole arc amplitude brings a reduction in the electromagnetic torque (Figure 3a) and torque ripples level (Figure 3b). The output power increases with increasing magnet width (Figure 3c); however, the magnet

width also provokes an increase in the peak-to-peak cogging torque, see Figure 3d. The demagnetization effects are covered in Figure 3e,f. The increase in the magnet width results in higher magnetic flux density, and consequently higher torque and power. However, this increase can critically cause demagnetization risks, which vary among the rotors, see Figure 3f, i.e., the R-IOW, R-SOW, and R-ROW arrangements have the highest magnetic field capability. This advantage becomes vital for high-speed applications because the risk of demagnetization significantly increases during full-load and high-speed operation.

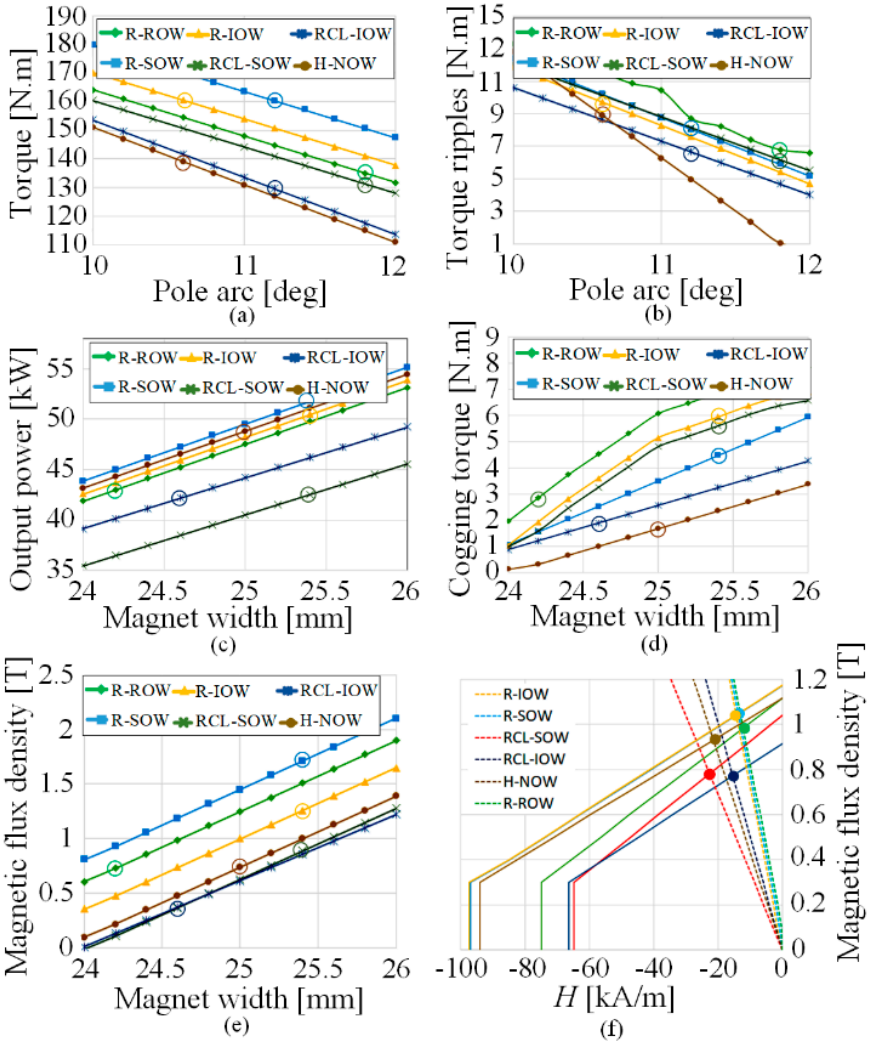

Figure 3. Sensitivity analysis for magnet sizing, in terms of: (**a**) electromagnetic torque as a function of pole arc, (**b**) electromagnetic toque ripples level as a function of pole arc, (**c**) output power as a function of magnet width, (**d**) cogging torque as a function of magnet width, (**e**) magnetic flux density as a function of magnet width, and (**f**) demagnetization curves for the considered PM arrangements. The circles highlight the selected parameter values for each configuration.

For fairness of comparison, the main magnet parameters for the considered arrangements have been selected through sensitivity analysis, as a trade-off in terms of electromagnetic performance, while accounting for saturation rating. The selected parameters are reported in Table 2, which includes ranges for the parameters that vary among the configurations. The axial length of the magnets is the same as the length of the rotor for all cases.

Table 2. Ranges of main rotor parameters for the considered PM arrangements.

Parameter	Description	Unit	Values
D_{ro}	Outer rotor diameter	mm	176.4
D_{ri}	Inner rotor diameter	mm	88
p	Number of poles	-	8
p_{arc}	Pole arc	deg	10–12
T_m	Magnet thickness	mm	6.5–8.5
T_1	Thickness of rotor yoke under the magnet	mm	33–35
L_m	Axial length of magnet	mm	74–84
V_m	Magnet volume	cm^3	24
V_p	Angular pitch	deg	45
W_m	Magnet width	mm	24–26

3. Mathematical Modeling of the IPMSMs

3.1. Finite Element Analysis Model

The objective of the simulation study is the electromagnetic evaluation of the magnet arrangements and their influence on *dq*-axis flux linkage, *dq*-axis synchronous inductance, back-electro-motive force (EMF), electromagnetic torque, as well as Joule and iron losses. The electromagnetic parameters are calculated with a 2-D FEA approach using the software package Flux. In the FEA simulations, constant settings are defined for: (i) the maximum root mean square (RMS) line current, provided by the inverter to the motor, set to 103 A, i.e., it is assumed that the operating limits of the powertrain are caused by the inverter; (ii) the maximum motor speed, i.e., $\omega_{max} = 10{,}000$ rpm; and (iii) the current coefficient, set to 0.8. Moreover, the speed range is discretized with steps of 10 rpm; the adopted airgap mesh density is 1.5; 100 operating points are considered per electrical torque period. Finally, steady-state thermal conditions are assumed. By supplying sinusoidal currents into the steady-state FEA model, the influence of the various magnet arrangements on the IPMSM performance is observed from the motor maps, which are generated over the whole motor speed (ω_{mot}) range, by applying the MTPA and MTPV strategies. The FEA simulation outputs several variables, the main ones being the magnetic flux density, B, and PM flux linkage, λ_m, which—in the post-processing phase—are used to calculate the *d*- and *q*-axis components of the inductance, L_d and L_q, as well as the different motor loss components, through analytical formulations.

3.2. Main Analytical Formulations

In the steady-state *dq*-framework rotating with electrical frequency ω_e [22], the voltage equations of the IPMSM are:

$$\begin{bmatrix} v_d \\ v_q \end{bmatrix} = \begin{bmatrix} R_s & -\omega_e L_q \\ \omega_e L_q & R_s \end{bmatrix} \begin{bmatrix} i_d \\ i_q \end{bmatrix} + \begin{bmatrix} 0 \\ \omega_e \lambda_m \end{bmatrix} \quad (1)$$

where v_d, v_q, i_d, and i_q are the *dq*-axis voltages and currents; and R_s is the stator winding resistance. i_d and i_q are related to the stator current, i_s, through the current angle β:

$$\begin{cases} i_d = -i_s \sin\beta \\ i_q = i_s \cos\beta \end{cases} \quad (2)$$

The electromagnetic and reluctance torque, T_e, is computed as:

$$T_e = \frac{3}{2} p \left[\lambda_m + \left(L_d - L_q\right) i_d\right] i_q \quad (3)$$

In the generation of the results, MTPA is adopted below the base speed, ω_b, while MTPV is used above ω_b. The MTPA algorithm is based on the solution of an optimization problem [22–25], which minimizes the continuous stator current, i_s, that generates the reference torque, T_{ref}, while meeting current and voltage constraints:

$$\begin{cases} \left[i_{d,MTPA}, i_{q,MTPA}\right] = \arg\min i_s^2 \\ \text{s.t.} \\ v_s \le \frac{V_{dc}}{\sqrt{3}} = V_{max} \\ i_s = \sqrt{i_d^2 + i_q^2} \le I_{max} \\ T_{ref} - T_e = 0 \end{cases} \tag{4}$$

where I_{max} is the stator current limit, which depends on the capability of the inverter; V_{max} is the stator voltage limit; V_{dc} is the DC (direct current) voltage of the inverter; and v_s is the magnitude of the stator voltage, given by:

$$v_s = \sqrt{v_d^2 + v_q^2} = \omega_e \sqrt{\left(L_q i_q\right)^2 + \left(L_d i_d + \lambda_m\right)^2} \tag{5}$$

The solution of the MTPA optimization problem results in the following current angle, β_{MTPA}, which was imposed in the generation of the motor maps through the FEA model:

$$\beta_{MTPA} = \sin^{-1} \frac{-\lambda_m + \sqrt{\lambda_m^2 + 8\left(L_q - L_d\right)^2 i_s^2}}{4\left(L_q - L_d\right) i_s} \tag{6}$$

MTPV is an effective strategy to obtain maximum torque when operating the motor in the flux weakening region, i.e., above the base speed [22–25]. The MTPV optimization problem can be formulated as:

$$\begin{cases} \left[i_{d,MTPV}, i_{q,MTPV}\right] = \arg\min v_s^2 \\ \text{s.t.} \\ v_s \le V_{max} \\ i_s \le I_{max} \\ T_{ref} - T_e = 0 \end{cases} \tag{7}$$

which, without considering core saturation, leads to:

$$i_{d,MTPV} = -\frac{\lambda_m}{L_d} + \frac{-L_q \lambda_m + \sqrt{\left(L_q \lambda_m\right)^2 + 4L_q^2\left(L_d - L_q\right)^2 i_q^2}}{2L_d\left(L_d - L_q\right)} \tag{8}$$

Condition (8) was imposed in the map generation process for $\omega_{mot} \ge \omega_b$.

The total motor power loss, $W_{mot,loss}$, is computed as the sum of the Joule loss W_J, iron loss W_{fe}, and mechanical loss W_{mech}:

$$W_{mot,loss} = W_J + W_{fe} + W_{mech} \tag{9}$$

where W_J is:

$$W_J = mR_{ph}\frac{i_d^2 + i_q^2}{2} = mR_{ph}I_{ph}^2 \tag{10}$$

In (10), m is the number of phases; R_{ph} is the phase resistance; and I_{ph} is the RMS value of the phase current. W_{fe} depends on the magnetic flux density, B. For each node of the iron loss mapping, B is output by a semi-numerical method based on the integration of the flux density in the airgap. B is computed as a function of the angular position θ, by

considering all relevant parts of the machine, i.e., the stator foot teeth, stator teeth, and yokes. A mathematical transformation is applied to obtain the time derivative of B for each speed interval:

$$\frac{dB(t)}{dt} = \frac{dB(\theta)}{d\theta}\frac{d\theta}{dt} \tag{11}$$

W_{fe} is given by:

$$\begin{aligned} W_{fe} = K_h K_f V_{fe} \quad & \left(\frac{B_{max}}{K_f}\right)^{\alpha_h} + K_c K_f V_{fe} \frac{1}{t_e} \int_0^{t_e} \left(\frac{1}{K_f}\frac{dB}{dt}\right)^{\alpha_c} dt \\ & + K_e K_f V_{fe} \frac{1}{t_e} \int_0^{t_e} \left(\frac{1}{K_f}\frac{dB}{dt}\right)^{\alpha_e} dt \end{aligned} \tag{12}$$

where K_h, K_c, K_e, and K_f are hysteresis, eddy-current, excessive, and stacking coefficients; α_h, α_c, and α_e are fitting constants for the hysteresis, eddy-current, and excessive terms; V_{fe} is the iron lamination volume; B_{max} is the maximum magnetic flux density; and t_e is the electrical period. W_{mech} is defined as:

$$W_{mech} = W_0 \left(\frac{\omega_{mot}}{\omega_{mot,0}}\right)^{K+1} \tag{13}$$

where W_0 is the mechanical loss at a reference speed; $\omega_{mot,0}$ is the nominal rotor speed; and K is the speed exponent. The magnitude of the mechanical loss is estimated for all motor configurations, and is the lowest for the R-SOW arrangement.

The motor efficiency, η_{mot}, is computed as:

$$\begin{aligned} \eta_{mot} \quad & = \frac{\omega_{mot} T_e - W_{mech} - W_{fe}}{\omega_{mot} T_e + W_J} = \frac{\omega_{mot} T_{mot}}{\omega_{mot} T_e + W_J} \\ & = \frac{\omega_{mot} T_{mot}}{\omega_{mot} T_{mot} + W_J + W_{mech} + W_{fe}} = \frac{\omega_{mot} T_{mot}}{\omega_{mot} T_{mot} + W_{mot,loss}} \end{aligned} \tag{14}$$

where T_{mot} is the mechanical torque at the motor shaft during steady-state operation.

4. Electromagnetic Performance Mapping of the IPMSMs

Based on the models in Section 3, the electromagnetic characteristics are generated as functions of flux linkage, across the whole speed-torque range. Table 3 reports the main electromagnetic properties for a current density of 6 A/mm^2. The produced magnetic field strength H (mean value) due to the permeances (with relative permeability of 1.1) and the flux per pole have their highest values in R-SOW, R-IOW, and H-NOW. The PM flux λ_m is particularly high for the R-IOW, R-SOW, and H-NOW arrangements, which are characterized by the lowest flux leakage. High values of the saliency ratio, ρ_{max}, such as those of the R-IOW and R-SOW arrangements, imply higher power capability and lower demagnetization, i.e., better high-speed performance. L_q has the highest values for RCL-SOW and RCL-IOW; moreover, the d-axis inductance L_d of RCL-SOW and RCL-IOW is rather high because the magnet is cut into two parts, which ultimately results in lower ρ_{max}. Figure 4 reports the flux linkage as a function of rotor position, with the highest magnitude shown by R-IOW and RCL-SOW, followed by R-ROW. Results of fast Fourier transform analysis show total harmonic distortions for the studied magnet arrangements ranging from 9.28 to 11.26%, with the lowest values belonging to R-SOW and R-IOW.

Figure 5 includes the iron loss maps at 6000 rpm, as functions of the dq-axis currents. Each map is divided into four quadrants, defined by dashed lines in the plots. In particular, for all layouts, the maximum iron losses are in the quadrant with dq-axis currents in the ranges $-100\ \text{A} \leq I_d \leq -50\ \text{A}$ and $0\ \text{A} \leq I_q \leq 50\ \text{A}$. The variations of the shape of the iron loss iso-lines highlight that the current amplitude and its angle are highly dependent on the magnet arrangement, which affects the power-related computations in the entire operating range. In general, the lowest maximum iron losses occur for R-ROW, RCL-SOW, and RCL-IOW.

Table 3. Electromagnetic characteristics of the considered PM arrangements for a current density of 6 A/mm^2.

Configuration	H [A/m]	Flux/Pole [mWb]	λ_m [Wb]	L_q [mH]	ρ_{max} [-]
R-ROW	74,823	4.18	0.103	32.52	2.15
R-SOW	96,987	4.62	0.130	29.89	2.45
R-IOW	99,146	4.61	0.132	31.62	2.44
RCL-SOW	64,746	3.32	0.092	38.44	2.29
RCL-IOW	66,328	3.31	0.093	39.94	2.31
H-NOW	94,065	4.74	0.115	29.05	2.28

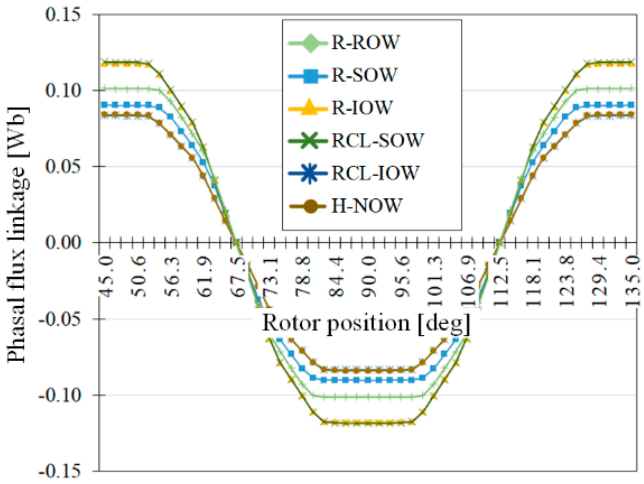

Figure 4. Phase flux linkage as a function of rotor position for the considered magnet arrangements.

Figure 6 presents the total loss maps as functions of torque, while Table 4 reports the RMS value of the phase current I_{ph}, as well as the Joule loss W_J, iron loss W_{fe}, mechanical loss W_{mech}, and total loss $W_{mot,loss}$, resulting from (9)–(13), at the maximum speed and torque of each configuration. For facilitating the visual analysis, the maps in Figure 6 subdivide the operating speed range of the motor into the following three regions, namely: (i) the starting-torque low-speed (ST-LS) region, below the base speed of the machine; (ii) the torque attenuation phase (AP), where the maximum torque is subject to a rather steep reduction with speed. This region covers the intermediate range of available speeds; and (iii) the highway driving high-speed region (HD-HS), covering the top range of achievable speeds of the machine, where the maximum torque reduction with speed is more moderate than in (ii). Depending on the vehicle type and application, the performance can be prioritized for different regions, e.g., the AP region can be the most significant one for a racing car, while the ST-LS region can be the most important one for an urban EV.

For example, the map for the R-ROW configuration in Figure 6a shows a constant torque range capability of 135 Nm, with a maximum loss of 1084 W at the base speed. In the AP speed range, the torque is subject to a significant reduction, with a maximum loss of 1807 W at 65 Nm and 6000 rpm. Under HD-HS operation, the total loss reaches 3750 W at 10,000 rpm, speed at which the maximum torque is ~30 Nm. In the R-SOW configuration in Figure 6b, the total losses are higher than for the R-ROW layout across the entire speed range; however, the torque production has considerably increased to 158 Nm, with a ~1300 W maximum loss at the base speed. During HD-HS operation, the torque capability is slightly higher than for R-ROW, but this corresponds to an increase in total loss, reaching a value in excess of 4000 W. Similar analyses can be made for all configurations.

Figure 7 reports the resulting power efficiency maps. All configurations have a region with efficiency values in excess of 0.97 at medium-to-high torque, for a speed range across the ST-LS and AP sectors. Such premium efficiency region covers a relatively small torque range in R-ROW, RCL-SOW, and RCL-IOW, and a wider torque range in R-SOW, R-IOW,

and H-NOW, while the speed range of the top efficiency region is rather similar for all maps. During high-speed operation, i.e., in the HD-HS range, the power efficiency of all configurations significantly decreases to values well below 0.90, and in some cases below 0.80.

Table 5 summarizes the electromagnetic performance of the considered configurations, with the following highlights: (i) the peak phase voltage is the highest in the R-SOW configuration, followed by R-IOW and H-NOW; (ii) the energy production of the permanent magnets is the highest for R-IOW, followed by R-SOW and H-NOW; (iii) at ω_b, the highest power is produced by R-SOW, R-IOW, and H-NOW. The maximum output power at ω_b is subject to a major variation depending on the rotor configuration, and ranges from ~42.3 to ~51.7 kW, i.e., the EV with the considered set of motors will have very different longitudinal acceleration performance characteristics; (iv) at ω_{max}, the top power capability is provided by R-SOW, followed by R-IOW; (v) the usable torque per magnet volume, i.e., T_e/V_m, is the highest for R-SOW at ω_b and ω_{max}; and (vi) R-SOW has the highest maximum efficiency at ω_b, while H-NOW has the highest maximum motor efficiency at ω_{max}. In general, based on the table and Figures 6 and 7, the R-SOW and R-IOW configurations, followed by H-NOW, appear to have overall desirable characteristics in terms of torque density production and premium efficiency area, which would make them good candidates for EV implementation.

To complete the analysis, Figure 8 shows the steady-state temperature distributions in the rotors, based on the FEA model results at the peak torque and base speed, and includes iso-temperature lines. The maximum temperatures are rather uniform among the magnet arrangements, with approximately 4 °C variations among the configurations. The lowest maximum temperature, equal to 64.5 °C, occurs for the H-NOW arrangement.

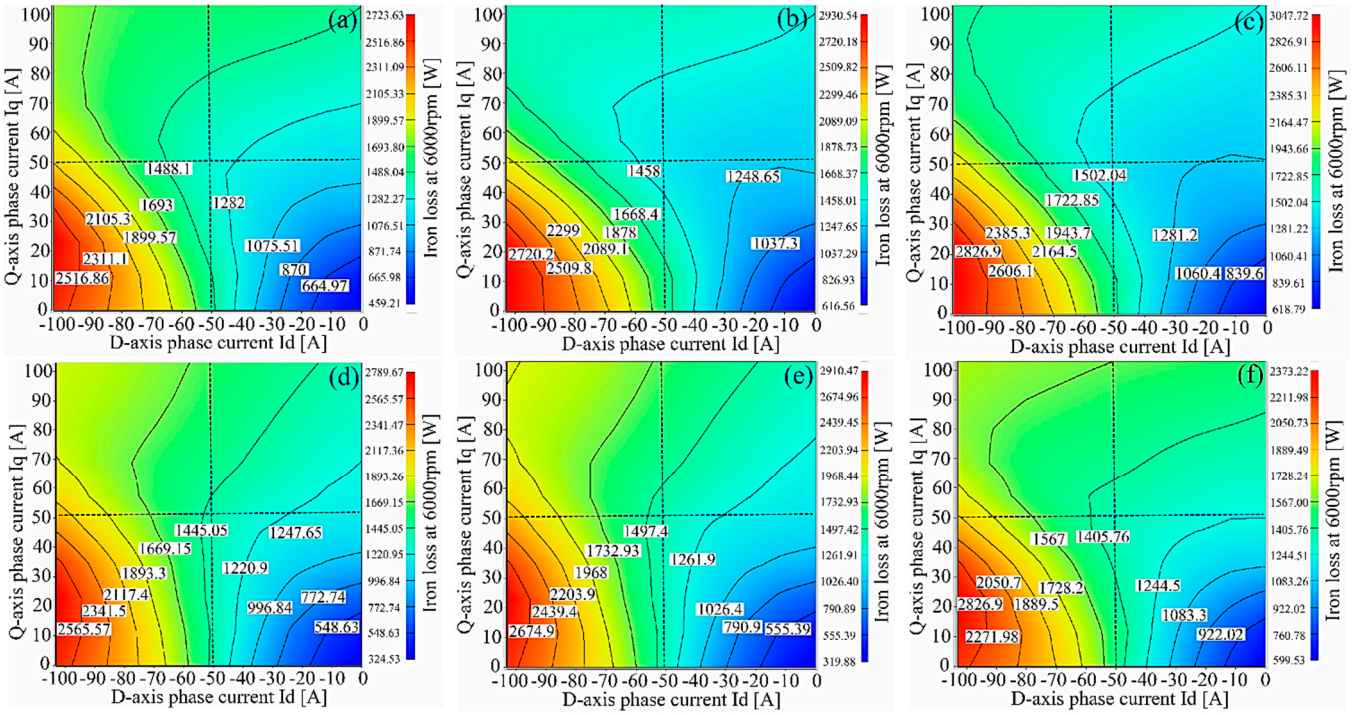

Figure 5. Iron loss maps at 6000 rpm for the IPMSM with (**a**) R-ROW, (**b**) R-SOW, (**c**) R-IOW, (**d**) RCL-SOW, (**e**) RCL-IOW, and (**f**) H-NOW arrangements.

Table 4. Phase current and losses at the maximum speed, under flux weakening conditions, for the considered arrangements.

Configuration	I_{ph} [A]	W_j [W]	W_{fe} [W]	W_{mech} [W]	$W_{mot,loss}$ [W]
R-ROW	51.6	195	3281	524	4000
R-SOW	72.8	389	3104	508	4001
R-IOW	71.0	369	3051	530	3950
RCL-SOW	54.0	213	2915	572	3700
RCL-IOW	53.1	207	3161	584	3952
H-NOW	65.2	311	3154	536	4001

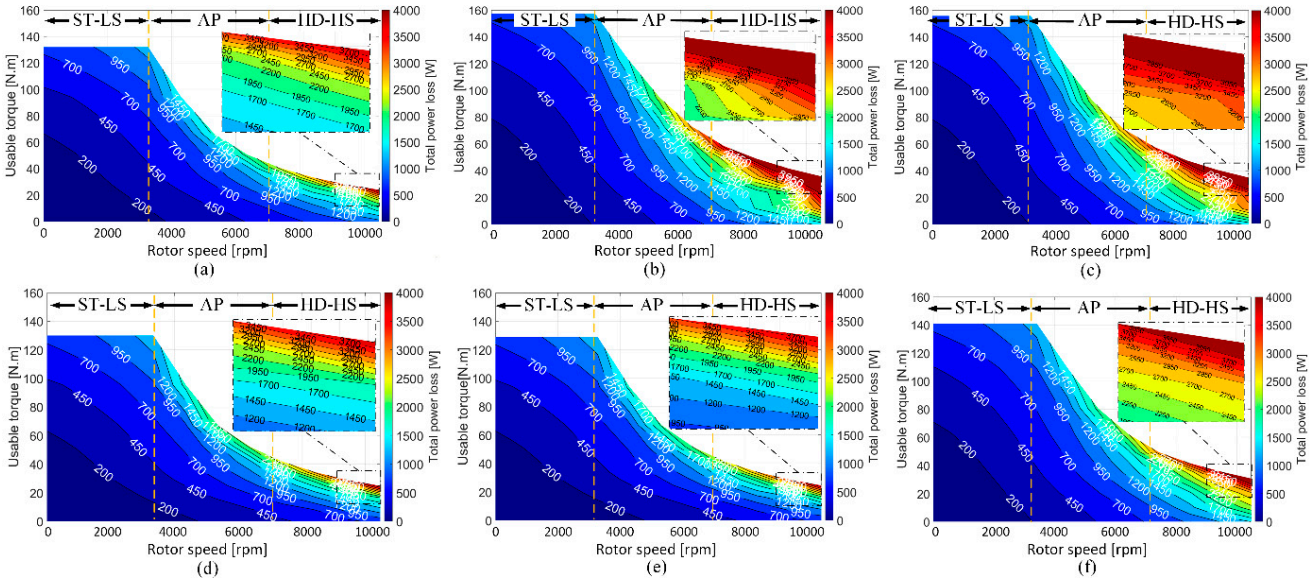

Figure 6. Total loss maps for the IPMSM with (**a**) R-ROW, (**b**) R-SOW, (**c**) R-IOW, (**d**) RCL-SOW, (**e**) RCL-IOW, and (**f**) H-NOW arrangements.

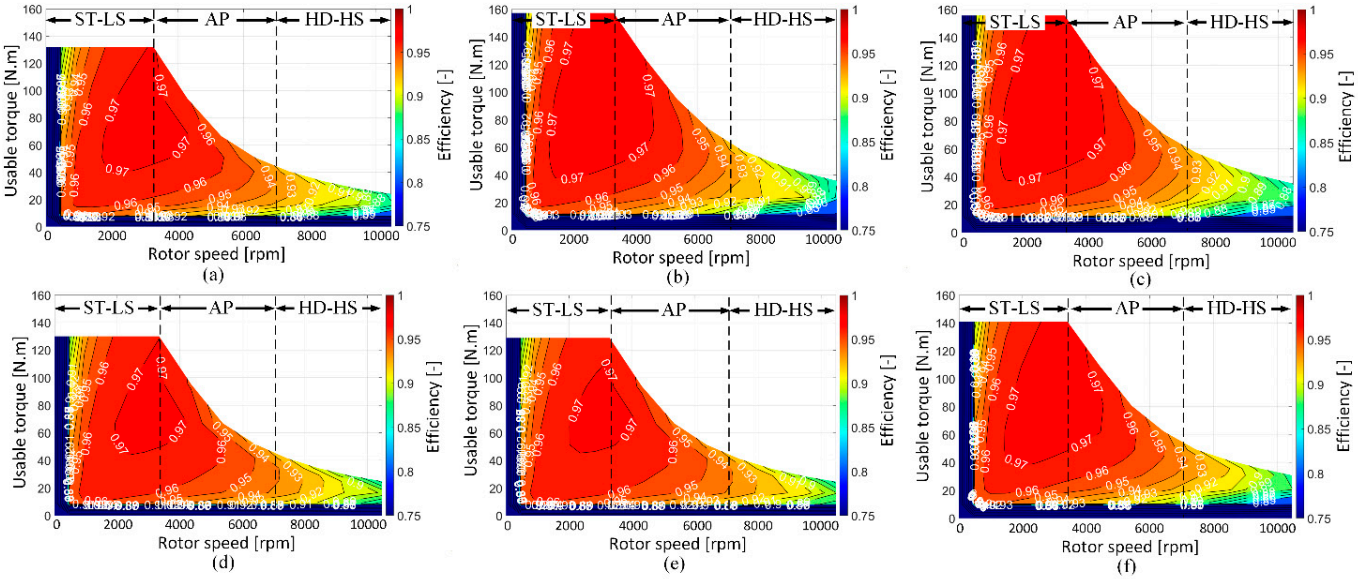

Figure 7. Power efficiency maps for the IPMSM with (**a**) R-ROW, (**b**) R-SOW, (**c**) R-IOW, (**d**) RCL-SOW, (**e**) RCL-IOW, and (**f**) H-NOW arrangements.

Table 5. Comparative summary of electromagnetic performance of the considered arrangements.

Key Parameters	R-ROW	R-SOW	R-IOW	RCL-SOW	RCL-IOW	H-NOW
Peak phase voltage	60.5	**68.8**	68.7	47.2	47.1	68.6
Energy production [kJ]	35.597	45.178	**46.074**	31.305	32.025	44.317
Output power at ω_b [kW]	43.091	**51.725**	50.661	43.476	42.334	48.073
Output power at ω_{max} [kW]	25.096	**37.401**	36.602	25.946	25.712	32.177
Power factor at ω_{max}	0.8348	0.8822	**0.8876**	0.8220	0.8278	0.8366
Flux weakening capability	Medium	Medium	Low	Medium	Medium	Low
Max. temperature at ω_b [°C]	68.7	67.2	67.2	65	65	**64.5**
Power losses for ST-LS	**Low**	**Low**	**Low**	**Low**	**Low**	High
Power losses for AP	**Low**	High	Medium	Medium	Medium	High
Power losses for HD-HS [-]	Medium	High	High	Medium	Medium	High
Torque ripple [%]	6.73	7.33	8.29	**5.81**	6.54	9.66
T_e/V_m at ω_{max} [Nm/cm^3]	0.685	**1.134**	0.999	0.738	0.628	0.978
T_e/V_m at ω_b [Nm/cm^3]	3.772	**4.492**	4.446	3.715	3.683	4.028
Max. efficiency at ω_b	0.9707	**0.9758**	0.9748	0.9699	0.9688	0.9734
Max. efficiency at ω_{max}	0.8632	0.8609	0.8592	0.8666	0.8668	**0.8734**

Notes: Bold text indicates the best performance among the considered arrangements, whereas underlined text indicates the worst performance.

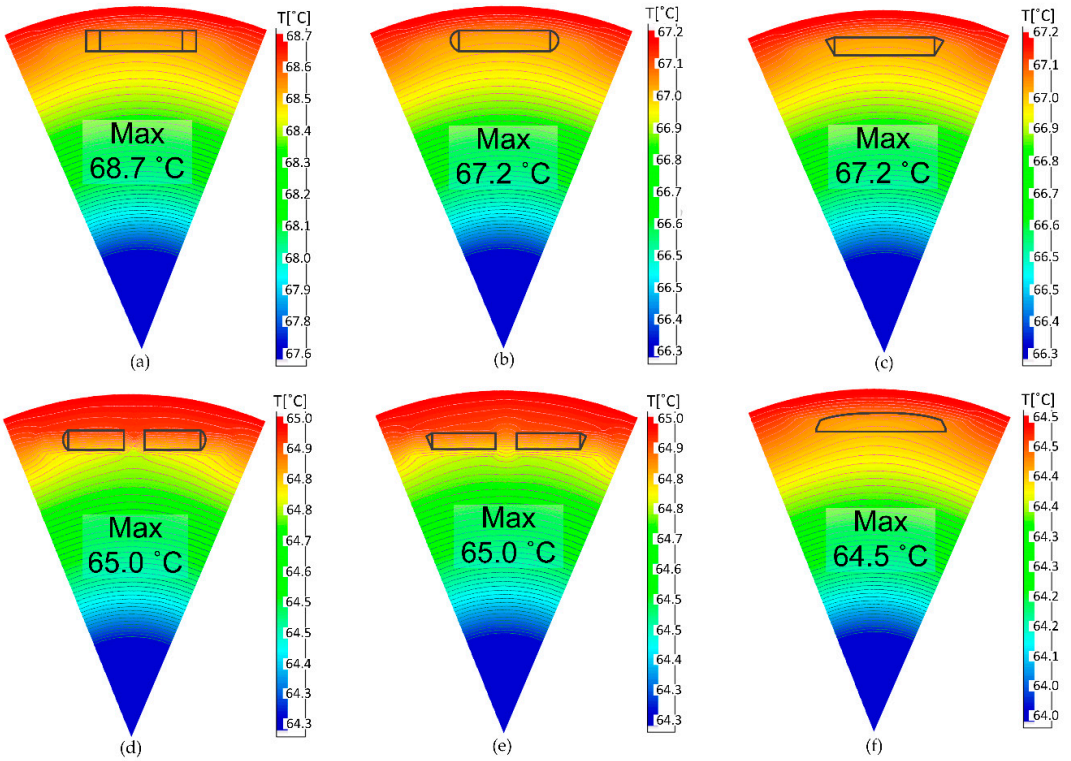

Figure 8. Temperature distribution in the considered IPMSM rotors with (**a**) R-ROW, (**b**) R-SOW, (**c**) R-IOW, (**d**) RCL-SOW, (**e**) RCL-IOW, and (**f**) H-NOW arrangements.

5. Electric Vehicle Simulation Results and Discussion

5.1. Case Study Vehicle

The case study EV is a light four-wheel-drive electric car, with two identical on-board IPMSMs, one per axle. The four-wheel-drive powertrain layout with central motors is becoming rather common in recent electric vehicles, see [14,43,44], as it conjugates a

simple configuration of the individual powertrains (see [45] for an example of powertrain optimization study) with the enhanced performance of a four-wheel-drive system. Each IPMSM is connected to the two wheels of the axle through a single-speed mechanical transmission with open differential, half-shafts, and constant velocity joints, according to the schematic in Figure 9. The main vehicle parameters are in Table 6.

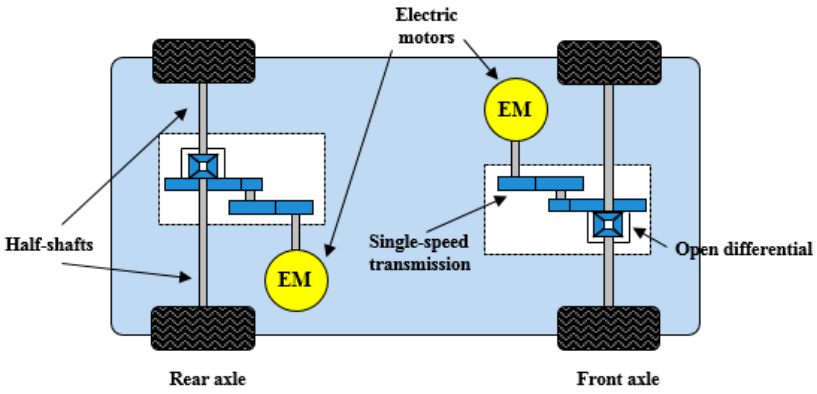

Figure 9. Schematic of the considered EV layout.

Table 6. Main EV parameters.

Parameters	Description	Unit	Value
m_0	Vehicle mass	kg	680
m_1	Payload	kg	200
A	Frontal area	m^2	2
L	Wheelbase	m	2.3
a	Front semi-wheelbase	m	1.3
H_{CG}	Center of gravity height	m	0.5
R_W	Wheel radius	m	0.3
C_d	Aerodynamic drag coefficient	-	0.35
C_{r0}	Rolling resistance coefficient (contribution independent from vehicle speed)	-	0.015
K	Rolling resistance coefficient (factor to be multiplied by vehicle speed squared)	s^2/m^2	6.5×10^{-6}

5.2. Driving Cycle Simulation

By using the power loss maps in Figure 6, the motor performance for each magnet arrangement is analyzed in terms of energy efficiency during traction along multiple driving cycles, representative of a wide range of operating conditions, namely: (i) the New European Driving Cycle (NEDC); (ii) the Worldwide harmonized Light vehicle Test Procedure (WLTP) Class 2; (iii) the ARTEMIS urban cycle; and (iv) the ARTEMIS motorway cycle [46].

To emulate the operation along a driving cycle, the torque of each machine is calculated under the following assumptions: (i) the road has zero longitudinal gradient; (ii) the regenerative braking capability of the electric powertrains is neglected, i.e., only the friction brakes are used for slowing down the vehicle, and thus the efficiency performance of the motors is analyzed solely for traction conditions; (iii) the transmission efficiency is constant; and (iv) the torque is evenly distributed between the two motors.

Each motor torque, T_{mot}, is calculated through a backward facing approach:

$$T_{mot} = \begin{cases} \frac{1}{2}\frac{F_t R_W}{\eta_{trans} G_r}, & if\ F_t \geq 0 \\ 0, & if\ F_t < 0 \end{cases} \quad (15)$$

where R_W is the wheel radius; η_{trans} is the transmission efficiency; G_r is the transmission gear ratio; and F_t is the longitudinal force, given by the sum of the aerodynamic drag force, F_d, the rolling resistance force, F_r, and the inertial force, F_a:

$$F_t = F_d + F_r + F_a \tag{16}$$

where the individual force contributions are:

$$F_d = \frac{1}{2}\rho_{air} A C_d v^2 \tag{17}$$

$$F_r = C_r(m_0 + m_1)g \tag{18}$$

$$F_a = (m_0 + m_{app} + m_1)a_x \tag{19}$$

In (17)–(19), ρ_{air} is the air density; v is the vehicle speed; C_r is the rolling resistance coefficient, expressed as $C_r = C_{r0} + Kv^2$, see [47]; g is the gravitational acceleration; m_{app} is the apparent mass of the rotating components of the electric powertrains; and a_x is the longitudinal vehicle acceleration. In the phases of the driving cycles in which $v = 0$, the condition $F_r = 0$ is imposed.

Through (15)–(19), the operating motor profiles along the considered driving cycles, i.e., the time histories of motor torque and speed, are calculated and represented on the power loss map. The interpolation of the speed and traction torque values on the motor maps brings the total motor power loss profile in traction, $W_{mot,loss}(t)$, from which, through time integration, the motor energy loss along the driving cycle, $E_{mot,loss}$, is obtained:

$$E_{mot,loss} = \int_{t_0}^{t_N} W_{mot,loss}(t)dt \approx \sum_{i=0}^{N-1} \frac{W_{mot,loss}(t_{i+1}) + W_{mot,loss}(t_i)}{2}(t_{i+1} - t_i) \tag{20}$$

where $t_0 = 0$ s and t_N are the initial and final times of the driving cycle; the subscript i defines the considered time step; and the index N represents the last step of the driving cycle. The total motor energy consumption along the cycle, $E_{mot,cons}$, is given by:

$$\begin{aligned} E_{mot,cons} &= E_{mot,traction} + E_{mot,loss} = \int_{t_0}^{t_N} T_{mot}(t)\omega_{mot}(t)dt + E_{mot,loss} \\ &\approx \sum_{i=0}^{N-1} \frac{T_{mot}(t_{i+1})\omega_{mot}(t_{i+1}) + T_{mot}(t_i)\omega_{mot}(t_i)}{2}(t_{i+1} - t_i) \\ &\quad + E_{mot,loss} \end{aligned} \tag{21}$$

where $E_{mot,traction}$ is the net traction energy of one motor, and $\omega_{mot} = vG_r/R_W$. The specific traction energy, $\overline{E}_{mot,traction}$, the specific energy loss, $\overline{E}_{mot,loss}$, and the specific energy consumption of the motor, $\overline{E}_{mot,cons}$, are obtained by dividing $E_{mot,traction}$, $E_{mot,loss}$, and $E_{mot,cons}$ by the driving cycle distance, d_{cycle}:

$$\overline{E}_{mot,traction} = \frac{E_{mot,traction}}{d_{cycle}} \tag{22}$$

$$\overline{E}_{mot,loss} = \frac{E_{mot,loss}}{d_{cycle}} \tag{23}$$

$$\overline{E}_{mot,cons} = \frac{E_{mot,cons}}{d_{cycle}} \tag{24}$$

The average energy efficiency of the traction motors along the driving cycle, $\overline{\eta}_{mot}$, is calculated as:

$$\overline{\eta}_{mot} = \frac{E_{mot,traction}}{E_{mot,cons}} = \frac{E_{mot,traction}}{E_{mot,traction} + E_{mot,loss}} \tag{25}$$

5.3. Longitudinal Acceleration and Road Gradient Performance Simulation

Under the assumption of high tire-road friction condition, i.e., with friction coefficient $\mu_{max} = 1.0$, the vehicle performance associated with the considered motor arrangements is evaluated in terms of:

- Maximum longitudinal acceleration from standstill, $a_{x,max}$, on a road with zero longitudinal gradient:

$$\begin{cases} a_{x,max} = \max\limits_{T_{mot,F}, T_{mot,R}} \frac{(T_{mot,F}+T_{mot,R})G_r\eta_{trans} - C_r(m_0+m_1)gR_W}{(m_0+m_{app}+m_1)R_W} \\ \text{s.t.} \\ T_{mot,F/R} \leq T_{mot,max} \\ \frac{F_{x,F/R}}{F_{z,F/R}} \leq \mu_{max} \end{cases} \tag{26}$$

  where the subscripts 'F' and 'R' refer to the front and rear axles; the notation $F_{x,F/R}$ indicates the front or rear longitudinal tire force in traction, calculated from the respective motor torque; and $F_{z,F/R}$ is the vertical load on the front or rear axle, which is a function of a_x, see [47] for the details. According to (26), the optimization results are calculated under the assumption that the front-to-total motor torque distribution can vary, according to the intervention of a traction controller that prevents wheel spinning on the critical axle. The results showed that for the specific vehicle the intervention of the traction controller is not required for maximum longitudinal acceleration in high tire-road friction conditions.
- Maximum longitudinal road gradient, ϑ_{max}, on which the vehicle can travel at very low speed (approaching zero) and zero longitudinal acceleration:

$$\begin{cases} \vartheta_{max} = \max\limits_{T_{mot,F}, T_{mot,R}} \vartheta \\ \text{s.t.} \\ \frac{(T_{mot,F}+T_{mot,R})G_r\eta_{trans}}{R_W} - (m_0+m_1)gsin(\vartheta) - C_r(m_0+m_1)gcos(\vartheta) = 0 \\ T_{mot,F/R} \leq T_{mot,max} \\ \frac{F_{x,F/R}}{F_{z,F/R}} \leq \mu_{max} \end{cases} \tag{27}$$

  In this case, it was verified that the traction controller has to intervene on the front axle for most motor configurations, i.e., the motor torque on the front axle has to be reduced to the level compatible with the tire-road friction condition.

5.4. Vehicle Simulation Results

Table 7 illustrates the motor and resulting vehicle performance characteristics. For the driving cycles, the table reports: (i) $\overline{E}_{mot,traction}$; (ii) $\overline{E}_{mot,loss}$; (iii) $\overline{E}_{mot,cons}$; (iv) $\overline{\eta}_{mot}$; (v) $\eta_{mot,avg}$, i.e., the average efficiency of each motor configuration along the four cycles; (vi) $\sigma_{\overline{\eta}_{mot}}$, i.e., the standard deviation of $\overline{\eta}_{mot}$ of each configuration along the cycles. Low values of $\sigma_{\overline{\eta}_{mot}}$ highlight consistent energy efficiency for the considered variety of driving conditions; (vii) η_{DC}, i.e., the average value of $\overline{\eta}_{mot}$ of all motor configurations, computed for each driving schedule; and (viii) $\sigma_{\eta_{DC}}$, i.e., the standard deviation of $\overline{\eta}_{mot}$ for all motor configurations, computed for each cycle. (i)–(vi) assess the efficiency performance of each motor configuration, while (vii) and (viii) provide an indication of the impact of the driving schedule on the results. Moreover, for the four cycles, the torque-speed diagrams in Figures 10–13 show the motor energy loss distributions for all cases. The white markers represent the operating points of the individual motors along the cycles. The magnitude of the energy losses in the corresponding torque-speed regions is indicated by the values in red as well as by the color maps, obtained by summing the energy losses of all operating points located in the region.

Table 7. Comparative summary of the performance of the case study EV with the considered IPMSM magnet arrangements.

Key Variables		R-ROW	R-SOW	R-IOW	RCL-SOW	RCL-IOW	H-NOW
Energy efficiency indicators							
$\overline{E}_{mot,traction}$ (W.h/km)	NEDC	54.67					
	WLTP class 2	44.48					
	ARTEMIS urban	52.05					
	ARTEMIS motorway	96.77					
$\overline{E}_{mot,loss}$ (W.h/km)	NEDC	3.85	4.72	4.70	3.21	**3.17**	4.52
	WLTP class 2	3.12	3.81	3.76	2.54	**2.51**	3.70
	ARTEMIS urban	2.60	2.81	2.79	2.37	**2.36**	2.82
	ARTEMIS motorway	7.42	9.10	9.49	6.46	**6.39**	8.46
$\overline{E}_{mot,cons}$ (W.h/km)	NEDC	58.52	59.39	59.36	57.88	**57.84**	59.19
	WLTP class 2	47.60	48.29	48.24	47.02	**46.98**	48.18
	ARTEMIS urban	54.65	54.86	54.84	54.42	**54.41**	54.87
	ARTEMIS motorway	104.18	105.86	106.26	103.23	**103.16**	105.23
$\overline{\eta}_{mot}$(-)	NEDC	0.9343	0.9206	0.9209	0.9445	**0.9452**	0.9236
	WLTP class 2	0.9344	0.9211	0.9220	0.9460	**0.9467**	0.9232
	ARTEMIS urban	0.9524	0.9487	0.9491	0.9564	**0.9565**	0.9486
	ARTEMIS motorway	0.9288	0.9141	0.9107	0.9374	**0.9381**	0.9196
$\eta_{mot,avg}$ (-)		0.9375	0.9261	0.9257	0.9461	**0.9466**	0.9288
$\sigma_{\overline{\eta}_{mot}}$ (-)		0.0089	0.0133	0.0142	0.0068	**0.0066**	0.0116
η_{DC} (-)	NEDC	0.9315					
	WLTP class 2	0.9322					
	ARTEMIS urban	0.9520					
	ARTEMIS motorway	0.9248					
$\sigma_{\eta_{DC}}$ (-)	NEDC	0.0105					
	WLTP class 2	0.0109					
	ARTEMIS urban	0.0034					
	ARTEMIS motorway	0.0107					
Vehicle performance indicators							
$a_{x,max}$ (m/s^2)		5.75	**6.87**	6.80	5.66	5.61	6.15
ϑ_{max} (deg)		35.0	**37.5**	37.4	34.8	34.7	35.9

Notes: Bold text indicates the best performance among the considered arrangements, whereas underlined text indicates the worst performance.

During the cycles, the motors mainly operate at low torque, i.e., at less than half of their maximum torque. The variety of driving conditions is confirmed by the spread of the $\overline{E}_{mot,cons}$ and $\overline{\eta}_{mot}$ values. For example, $\overline{E}_{mot,cons}$ along the WLTP is less than half than along the ARTEMIS motorway. The energy efficiency along the ARTEMIS urban is the highest among the four driving cycles for each magnet arrangement. In general, motor efficiency is characterized by a decrease in high speed conditions. The effect is confirmed by η_{DC}, which ranges from 0.9248 for the ARTEMIS motorway to 0.9520 for the ARTEMIS urban, indicating that the low speed operation typical of urban driving is favorable to efficiency. The highest significance of the magnet arrangement on energy consumption is obtained for the ARTEMIS motorway, with ~3% energy efficiency increase from the R-IOW to the RCL-IOW configurations.

Among all arrangements, RCL-IOW provides the highest energy efficiency along each selected driving cycle, and has the lowest energy loss not only in the peak-loss region, but also in most operating areas, see Figures 10–13, followed by RCL-SOW and R-ROW. The RCL-IOW set-up also shows the lowest energy efficiency standard deviation among the different cycles, and thus provides consistently low consumption in various driving conditions.

At the bottom end of the ranking, R-SOW has the lowest energy efficiency along the NEDC and WLTP, while H-NOW and R-IOW rank last along the ARTEMIS urban and

ARTEMIS motorway. The H-NOW arrangement, which was very promising according to the power efficiency map in Figure 7, is not competitive when realistic driving scenarios are investigated, although it exhibits high maximum efficiency for both the base and top speeds, see Table 5. On the contrary, the RCL-IOW arrangement, which in Table 5 has significantly lower maximum values of power efficiency than H-NOW, provides higher energy efficiency during driving cycle operation.

Interestingly, the results show that the observation of the power efficiency maps may be misleading for predicting the energy consumption performance along different driving conditions. This can be explained based on Figures 7 and 10, Figures 11–13, as most of the operating points of the considered driving cycles do not fall in the premium efficiency regions, but are rather at lower torque and higher speeds within the AP region, where the gradient of the motor efficiency characteristic, with respect to the variation of both speed and torque, becomes the most important aspect. The RCL-SOW and RCL-IOW configurations present indeed lower gradients of the power efficiency characteristic in comparison with the solutions with the widest premium efficiency regions, i.e., R-SOW and R-IOW.

The bottom half of Table 7 deals with the longitudinal acceleration and gradeability performance associated with each rotor configuration, and reports the values of $a_{x,max}$ and ϑ_{max}. The most energy-efficient configurations, e.g., RCL-IOW, are characterized by low values of torque for the considered maximum inverter current, thus providing sub-optimal drivability at low speed. Vice versa, the configurations with the highest maximum torque score worse in the energy consumption simulations. For example, below the base speed, a layout like R-IOW provides a maximum torque that is ~30 Nm higher than that for RCL-IOW, which is the most energy-efficient configuration. The correlation of the driving cycle results and electromagnetic analysis suggests that the low gradient of the efficiency map of the best performing motors along the cycles is associated with low flux densities, and thus low maximum torque capability. The important conclusion is that the rotor arrangement selection is a compromise between: (i) desirable acceleration and gradeability performance, requiring motor behavior optimized for high torque conditions, with high flux density; and (ii) energy efficiency along driving cycles, requiring low gradients in the relevant parts of the efficiency map, even at the price of narrower premium efficiency regions.

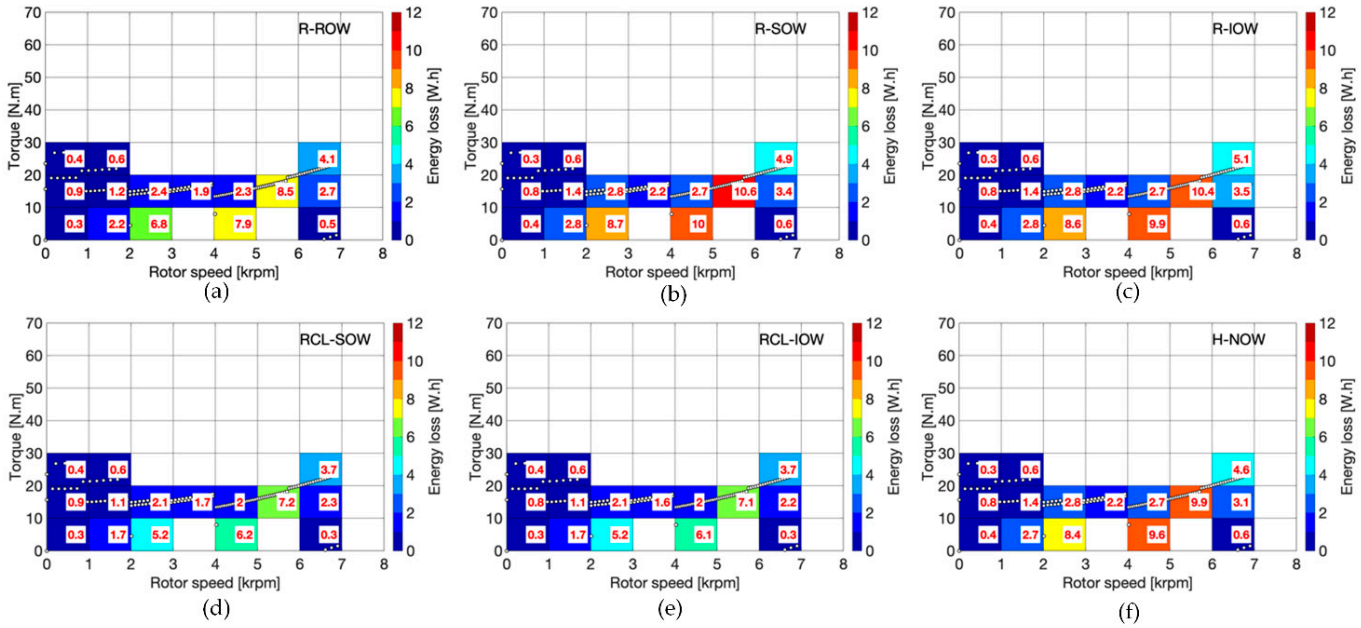

Figure 10. Energy loss distributions for the IPMSM with (**a**) R-ROW, (**b**) R-SOW, (**c**) R-IOW, (**d**) RCL-SOW, (**e**) RCL-IOW, and (**f**) H-NOW arrangements, along the NEDC driving cycle.

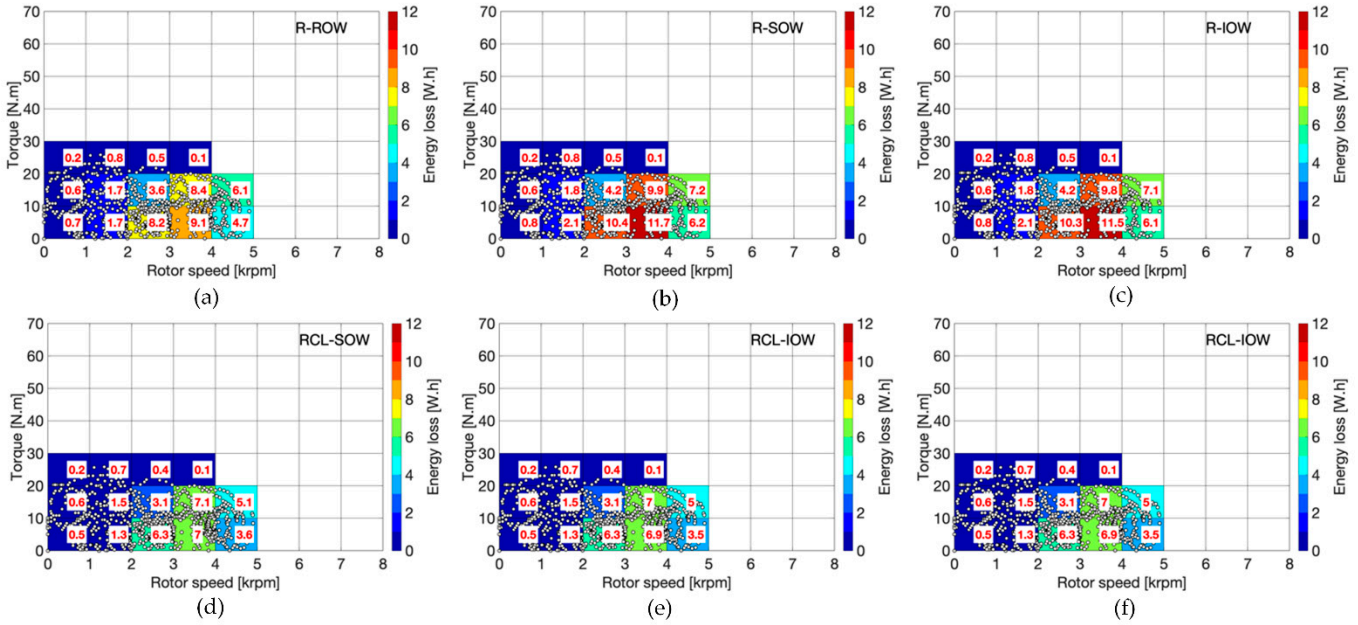

Figure 11. Energy loss distributions of the IPMSM with (**a**) R-ROW, (**b**) R-SOW, (**c**) R-IOW, (**d**) RCL-SOW, (**e**) RCL-IOW, and (**f**) H-NOW arrangements, along the WLTP Class 2 driving cycle.

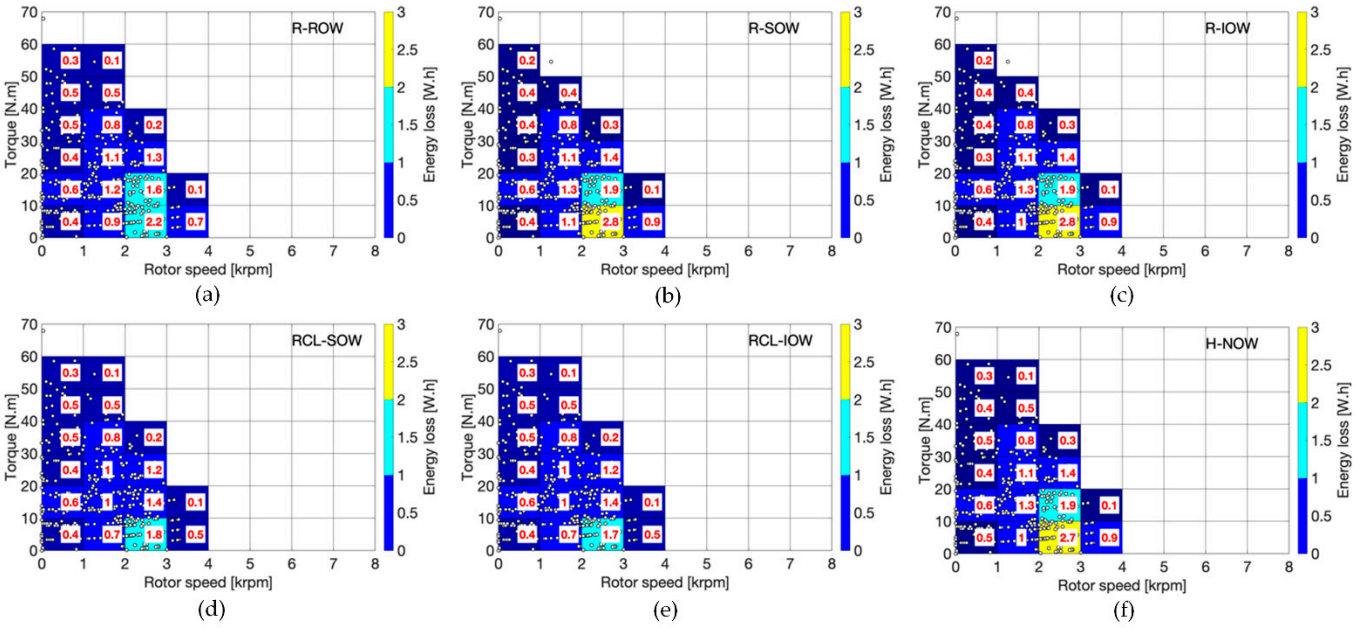

Figure 12. Energy loss distributions of the IPMSM with (**a**) R-ROW, (**b**) R-SOW, (**c**) R-IOW, (**d**) RCL-SOW, (**e**) RCL-IOW, and (**f**) H-NOW arrangements, along the ARTEMIS urban driving cycle.

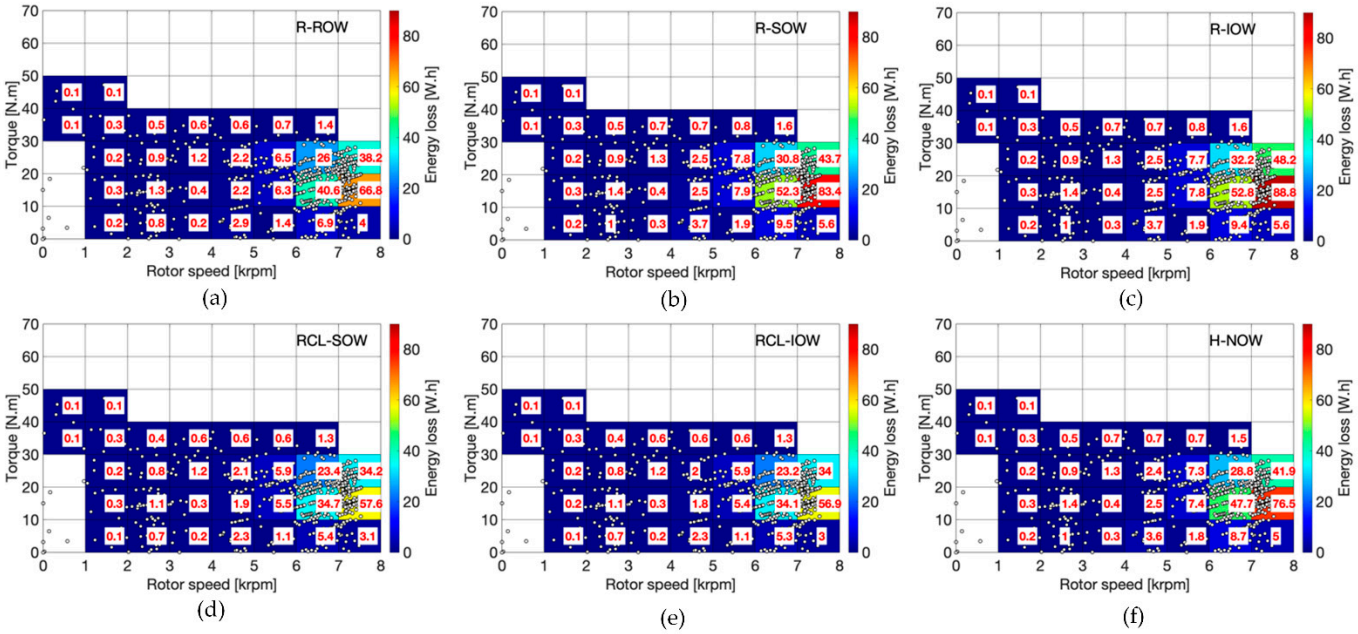

Figure 13. Energy loss distributions of the IPMSM with (**a**) R-ROW, (**b**) R-SOW, (**c**) R-IOW, (**d**) RCL-SOW, (**e**) RCL-IOW, and (**f**) H-NOW arrangements, along the ARTEMIS motorway driving cycle.

6. Conclusions

This study evaluated the influence of six buried magnet arrangements on the performance of a case study 48-slot 8-pole IPMSM for automotive traction applications, controlled through maximum-torque-per-ampere (MTPA) and maximum-torque-per-voltage (MTPV) strategies. The magnet sizing for each arrangement was based on the DOE/R sensitivity method, for a constant total magnet volume. The electromagnetic parameters for the rotor configurations were calculated through a two-dimensional finite element analysis approach, under the assumption of steady-state thermal conditions in the rotors. *dq*-axis modeling was adopted to analyze the performance of the IPMSMs with different rotor configurations, by using circuit equations that consider stator and PM flux linkages, as well as *d*- and *q*-axis inductances that are nonlinear functions of the flux level. The respective power loss and efficiency maps were generated over the entire torque-speed range. The performance of the considered IPMSMs was evaluated along four driving cycles, representative of urban and extra-urban driving conditions, as well as in terms of acceleration and gradeability, by simulating a light four-wheel-drive electric vehicle with two on-board motors and even wheel torque distribution among the two axles.

The main conclusions of the electric motor and vehicle simulation analyses are:

- The power efficiency values show major variations for the different motor configurations, especially at medium-to-high speed values. The premium efficiency region, i.e., with efficiency values in excess of 0.97, covers a small range, both in terms of torque and speed, for the R-ROW, RCL-SOW, and RCL-IOW configurations, and a slightly wider speed range with a significantly wider torque range in the R-SOW, R-IOW, and H-NOW layouts.
- For the considered maximum inverter current, the torque capability of the motor is significantly affected by the magnet arrangement; in fact, the maximum torque ranges from ~130 Nm for the RCL-IOW configuration to ~160 Nm for the R-SOW layout.
- As the power efficiency of the case study motors tends to significantly decrease with speed, the cycles with substantial urban driving sections provide higher energy efficiency, e.g., the average energy efficiency of the considered motors is 0.9248 along the ARTEMIS motorway cycle, and 0.9520 for the ARTEMIS urban.
- The energy efficiency along driving cycles is affected by the magnet arrangement, and can vary up to ~3% depending on the rotor configuration. The WLTP class 2

cycle originates the maximum standard deviation of the motor energy efficiency with the considered set of rotor layouts. The magnet configuration selection is crucial for traction motors of electric vehicles operating in a wide range of speeds, while it is less significant in urban driving, e.g., the standard deviation of the energy efficiency along the ARTEMIS urban is less than one third of the respective value along the ARTEMIS motorway.

- In typical driving schedules, the motors operate at relatively low torque, i.e., normally at less than half of their peak torque in the considered electric vehicle. Hence, the magnet arrangements providing high values of maximum efficiency for high torque at the base and top speeds, such as H-NOW, may not yield practical benefits along normal driving, while configurations with lower maximum efficiency at high torque, such as RCL-IOW, can be rather effective in realistic scenarios.
- With an average efficiency of 0.9466, the RCL-IOW layout is the most efficient configuration for the specific vehicle, followed by RCL-SOW and R-ROW, having average energy efficiencies of 0.9461 and 0.9375 along the selected schedules.
- For the given maximum inverter current, the longitudinal acceleration and gradeability performance is very strongly affected by the rotor arrangement, i.e., the maximum longitudinal acceleration at zero road gradient ranges from 5.61 to 6.87 m/s^2, and the maximum road gradient ranges from 34.7 to 37.5 deg, in high tire-road friction conditions.

Interestingly, the rotor configurations providing the best drivability performance are those with the lowest energy efficiency, and vice versa. Hence, the selection of the motor rotor configuration must be the result of a trade-off between drivability and energy efficiency, depending on the specific vehicle requirements, and cannot be based only on motor performance analysis results.

Future investigations will include: (i) more accurate modeling techniques for the machines, e.g., three-dimensional FEA approaches accounting for the axial length effects; (ii) optimal sizing of the magnets for each rotor arrangement; (iii) more advanced vehicle simulations, e.g., to include tire slip power losses; (iv) energy-efficient front-to-rear motor torque distribution algorithms, including regenerative braking functionalities; and (v) different electric powertrain topologies.

Author Contributions: For this research article, P.A., R.B., A.L. D.T., L.S. and A.S. have contributed to the investigation, methodology, resources, writing and editing, and supervision. The software simulations and visualizations were mainly carried out by P.A. and L.S. All authors have read and agreed to the published version of the manuscript.

Funding: This research received no external funding.

Institutional Review Board Statement: Not applicable.

Conflicts of Interest: The authors declare no conflict of interest. The funders had no role in the design of the study; in the collection, analyses, or interpretation of data; in the writing of the manuscript, or in the decision to publish the results.

References

1. Jahns, T.M.; Kliman, G.B.; Neumann, T.W. Interior Permanent-Magnet Synchronous Motors for Adjustable-Speed Drives. *IEEE Trans. Ind. Appl.* **1986**, *22*, 738–747. [CrossRef]
2. Yamazaki, K.; Kumagai, M.; Ikemi, T.; Ohki, S. A Novel Rotor Design of Interior Permanent-Magnet Synchronous Motors to Cope with Both Maximum Torque and Iron-Loss Reduction. *IEEE Trans. Ind. Appl.* **2013**, *49*, 2478–2486. [CrossRef]
3. Liu, X.; Wu, D.; Zhu, Z.Q.; Pride, A.; Deodhar, R.P.; Sasaki, T. Efficiency Improvement of Switched Flux PM Memory Machine Over Interior PM Machine for EV/HEV Applications. *IEEE Trans. Magn.* **2014**, *50*, 1–4. [CrossRef]
4. Williamson, S.; Lukic, M.; Emadi, A. Comprehensive drive train efficiency analysis of hybrid electric and fuel cell vehicles based on motor-controller efficiency modeling. *IEEE Trans. Power Electron.* **2006**, *21*, 730–740. [CrossRef]
5. Jiang, W.; Feng, S.; Zhang, Z.; Zhang, J.; Zhang, Z. Study of efficiency characteristics of interior permanent magnet synchronous motors. *IEEE Trans. Magn.* **2018**, *54*, 1–5. [CrossRef]

6. Bianchi, N.; Jahns, T. Design, analysis, and control of interior PM synchronous machines. In Proceedings of the IEEE-IAS Electrical Machines Committee, Seattle, WA, USA, 3–7 October 2004.
7. Hong, S.G.; Park, I.H. Continuum-Sensitivity-Based Optimization of Interior Permanent Magnet Synchronous Motor with Shape Constraint for Permanent Magnet. *IEEE Trans. Magn.* **2020**, *56*, 1–4. [CrossRef]
8. Du, J.; Wang, X.; Lv, H. Optimization of Magnet Shape Based on Efficiency Map of IPMSM for EVs. *IEEE Trans. Appl. Supercond.* **2016**, *26*, 1–7. [CrossRef]
9. Kwak, S.; Kim, J.; Jung, H. Characteristic analysis of multilayer buried magnet synchronous motor using fixed permeability method. *IEEE Trans. Energy Convers.* **2005**, *20*, 549–555. [CrossRef]
10. Kim, K.C.; Kim, K.; Kim, H.J.; Lee, J. Demagnetization Analysis of Permanent Magnets According to Rotor Types of Interior Permanent Magnet Synchronous Motor. *IEEE Trans. Magn.* **2009**, *45*, 2799–2802. [CrossRef]
11. Cirani, M.; Eriksson, S.; Thunberg, J. Innovative Design for Flux Leakage Reduction in IPM Machines. *IEEE Trans. Ind. Appl.* **2014**, *50*, 1847–1853. [CrossRef]
12. Kano, Y. Torque Ripple Reduction of Saliency-Based Sensorless Drive Concentrated-Winding IPMSM Using Novel Flux Bar-rier. *IEEE Trans. Ind. Appl.* **2015**, *51*, 2905–2916. [CrossRef]
13. Zhu, Z.; Wang, K.; Ombach, G. Optimal magnet shaping with third order harmonic for maximum torque in brushless AC machines. In Proceedings of the 6th IET International Conference on Power Electronics, Machines and Drives (PEMD 2012), Bristol, UK, 27–29 March 2012.
14. Shao, L.; Karci, A.E.H.; Tavernini, D.; Sorniotti, A.; Cheng, M. Design Approaches and Control Strategies for Energy-Efficient Electric Machines for Electric Vehicles—A Review. *IEEE Access* **2020**, *8*, 116900–116913. [CrossRef]
15. Dlala, E.; Solveson, M.G.; Stanton, S.; Tang, Z.; Christini, M.; Ong, R.; Peaslee, B. Efficiency map simulations for an interior PM motor with experimental comparison and investigation of magnet size reduction. In Proceedings of the 2013 International Electric Machines & Drives Conference, Chicago, IL, USA, 12–15 May 2013.
16. Mohammadi, M.; Lowther, D. A computational study of efficiency map calculation for synchronous AC motor drives including cross coupling and saturation effects. *IEEE Trans. Magn.* **2017**, *53*, 1–4. [CrossRef]
17. Zhou, X.; Zhou, Y.; Wang, H.; Lu, M.; Zeng, F.; Yu, Y. An Improved MTPA Control Based on Amplitude-Adjustable Square Wave Injection. *IEEE Trans. Energy Convers.* **2020**, *35*, 956–965. [CrossRef]
18. Wang, G.; Li, Z.; Zhang, G.; Yu, Y.; Xu, D. Quadrature PLL-based high-order sliding-mode observer for IPMSM sensorless control with online MTPA control strategy. *IEEE Trans. Energy Convers.* **2013**, *28*, 214–224. [CrossRef]
19. Pan, C.T.; Sue, S.M. A Linear Maximum Torque Per Ampere Control for IPMSM Drives Over Full-Speed Range. *IEEE Trans. Energy Convers.* **2005**, *20*, 359–366. [CrossRef]
20. Mohamed, Y.; Lee, T. Adaptive self-tuning MPTA vector controller for IPMSMs drive system. *IEEE Trans. Energy Convers.* **2006**, *21*, 636–644. [CrossRef]
21. Liu, Q.; Hameyer, K. High-Performance Adaptive Torque Control for an IPMSM With Real-Time MTPA Operation. *IEEE Trans. Energy Convers.* **2017**, *32*, 571–581. [CrossRef]
22. Lemmens, J.; Vanassche, P.; Driesen, J. PMSM Drive Current and Voltage Limiting as a Constraint Optimal Control Problem. *IEEE J. Emerg. Sel. Top. Power Electron.* **2014**, *3*, 326–338. [CrossRef]
23. Cheng, B.; Tesch, T.R. Torque Feedforward Control Technique for Permanent-Magnet Synchronous Motors. *IEEE Trans. Ind. Electron.* **2010**, *57*, 969–974. [CrossRef]
24. Sun, J.; Lin, C.; Xing, J.; Jiang, X. Online MTPA Trajectory Tracking of IPMSM Based on a Novel Torque Control Strategy. *Energies* **2019**, *12*, 3261. [CrossRef]
25. Xia, Z.; Nalakath, S.; Tavirdilu-Asl, R.; Sun, Y.; Wiseman, J.; Emadi, A. Online Optimal Tracking Method for Interior Permanent Magnet Machines with Improved MTPA and MTPV in Whole Speed and Torque Ranges. *IEEE Trans. Power Electron.* **2020**, *35*, 9753–9769. [CrossRef]
26. Wang, X.; Kennel, R.; Xie, W.; Gerling, D. Analysis of losses in a novel IPMSM resulting from high-frequency injection for sensorless control. In Proceedings of the 2013 IEEE International Symposium on Sensorless Control for Electrical Drives and Predictive Control of Electrical Drives and Power Electronics (SLED/PRECEDE), Munich, Germany, 17–19 October 2013.
27. Kulkarni, S.; Pendse, A.; Wagh, P.; Sonawane, M.; Pawaskar, O.; Bhawalkar, M.; Kulkarni, M. Production Friendly Design and Development of Brushless DC Machines. In Proceedings of the 19th International Conference on Electrical Machines and Systems (ICEMS), Chiba, Japan, 13–16 November 2016.
28. Kano, Y.; Kosaka, T.; Matsui, N.; Nakanishi, T. A New Technique of Torque Ripple Reduction in Saliency-Based Sensor-less Drive IPM Motors for General Industrial Applications. In Proceedings of the 13th European Conference on Power Electronics and Applications, Barcelona, Spain, 8–10 September 2009.
29. Kano, Y. Sensorless-oriented design of IPMSM. In Proceedings of the 2014 International Power Electronics Conference (IPEC-Hiroshima 2014—ECCE ASIA), Hiroshima, Japan, 18–21 May 2014.
30. Liu, X.; Lin, Q.; Fu, W. Optimal Design of Permanent Magnet Arrangement in Synchronous Motors. *Energies* **2017**, *10*, 1700. [CrossRef]
31. Dong, J.; Huang, Y.; Jin, L.; Lin, H. Comparative Study of Surface-Mounted and Interior Permanent-Magnet Motors for High-Speed Applications. *IEEE Trans. Appl. Supercond.* **2016**, *26*, 1–4. [CrossRef]

32. Sayed, E.; Yang, Y.; Bilgin, B.; Bakr, M.H.; Emadi, A. A Comprehensive Review of Flux Barriers in Interior Permanent Magnet Synchronous Machines. *IEEE Access* **2019**, *7*, 149168–149181. [CrossRef]
33. Thike, R.; Pillay, P. Mathematical Model of an Interior PMSM with Aligned Magnet and Reluctance Torques. *IEEE Trans. Transp. Electrification* **2020**, *6*, 647–658. [CrossRef]
34. Balasubramanian, S.; Heister, C.; Henke, M. Design Guidelines for Synchronous Machine Topologies with High Torque and Wide Field Weakening Demands. In Proceedings of the 2019 IEEE International Electric Machines & Drives Conference (IEMDC), San Diego, CA, USA, 12–15 May 2019.
35. Imoto, R.; Sanada, M.; Morimoto, S.; Inoue, Y. Study on Rotor Structure Suitable for Improving Power Density and Efficiency in IPMSMs for Automotive Applications. In Proceedings of the International Power Electronics Conference (IPEC-Niigata 2018 -ECCE Asia), Niigata, Japan, 20–24 May 2018.
36. Yoshioka, S.; Morimoto, S.; Sanada, M.; Inoue, Y. Influence of magnet arrangement on the performance of IPMSMs for automotive applications. In Proceedings of the 2014 IEEE Energy Conversion Congress and Exposition (ECCE), Chiba, Japan, 14–18 September 2014.
37. Shimizu, Y.; Morimoto, S.; Sanada, M.; Inoue, Y. Influence of Permanent Magnet Properties and Arrangement on Performance of IPMSMs for Automotive Applications. In Proceedings of the 19th International Conference on Electrical Machines and Systems (ICEMS), Chiba, Japan, 13–16 November 2016.
38. Liu, C.T.; Hwang, C.C. Design and Construction of an IPM Motor for Automatic Tapping Machine Tool Applications. In Proceedings of the 2019 IEEE International Electric Machines & Drives Conference (IEMDC), San Diego, CA, USA, 12–15 May 2019.
39. Jung, J.W.; Lee, S.H.; Lee, G.H.; Hong, J.P.; Lee, D.H.; Kim, K.N. Reduction Design of Vibration and Noise in IPMSM Type Integrated Starter and Generator for HEV. *IEEE Trans. Magn.* **2010**, *46*, 2454–2457. [CrossRef]
40. Zhang, P.; Sizov, G.Y.; He, L.; Ionel, D.M.; Dernerdash, N.A.D. Calculation of Magnet Losses in Concentrated-Winding Permanent Magnet Synchronous Machines Using a Computationally Efficient—Finite Element Method. *IEEE Trans. Ind. Appl.* **2013**, *49*, 2524–2532. [CrossRef]
41. Matsumoto, Y.; Miki, I.; Morinaga, K. Study on IPMSM with Ferrite Magnets Driven at High Speeds. In Proceedings of the IEEE International Conference on Electrical Machines and Systems, Busan, Korea, 26–29 October 2013.
42. Asef, P.; Lapthorn, A. Overview of Sensitivity Analysis Methods Capabilities for Traction AC Machines in Electrified Vehicles. *IEEE Access* **2021**, *9*, 23454–23471. [CrossRef]
43. De Pinto, S.; Camocardi, P.; Chatzikomis, C.; Sorniotti, A.; Bottiglione, F.; Mantriota, G.; Perlo, P. On the Comparison of 2- and 4-Wheel-Drive Electric Vehicle Layouts with Central Motors and Single- and 2-Speed Transmission Systems. *Energies* **2020**, *13*, 3328. [CrossRef]
44. Huynh, T.A.; Hsieh, M.F. Performance Analysis of Permanent Magnet Motors for Electric Vehicles (EV) Traction Considering Driving Cycles. *Energies* **2018**, *11*, 1385. [CrossRef]
45. Sieklucki, G. Optimization of Powertrain in EV. *Energies* **2021**, *14*, 725. [CrossRef]
46. Emission Test Cycles. Available online: https://dieselnet.com/standards/cycles/index.php (accessed on 2 March 2021).
47. Genta, G. *Motor Vehicle Dynamics: Modeling and Simulation*; World Scientific Publishing: Singapore, 1997; Volume 43, pp. 1–600.